

**A lidar and backscatter sonde aerosol measurement campaign
at Table Mountain during February–March 1997: Observations
of stratospheric background aerosols and cirrus clouds**

G. Beyerle,^{1,8} M. R. Gross,² D. A. Haner,³ N. T. Kjome,⁴ I. S. McDermid,¹
T. J. McGee,⁵ J. M. Rosen,⁴ H.-J. Schäfer,^{6,7} and O. Schrems⁶

Short title: AEROSOL LIDAR MEASUREMENT CAMPAIGN

¹Jet Propulsion Laboratory, California Institute of Technology, Wrightwood CA, USA

²University of Maryland, Baltimore County MD, USA

³California State Polytechnic University, Pomona CA, USA

⁴University of Wyoming, Laramie WY, USA

⁵Goddard Space Flight Center, Greenbelt MD, USA

⁶Alfred Wegener Institute for Polar and Marine Research, Bremerhaven, Germany

⁷now with INNOSOFT GmbH, Köln, Germany

⁸now at Alfred Wegener Institute for Polar and Marine Research, Potsdam, Germany

Abstract. Results from an aerosol measurement campaign performed at Table Mountain Facility / Jet Propulsion Laboratory / California Institute of Technology (34.4°N, 117.7°E, 2280 m asl) in February–March 1997 are presented. Three aerosol lidar instruments participated in the campaign: the Aerosol-Temperature-Lidar (AT-lidar) from Goddard Space Flight Center, the Mobile-Aerosol-Raman-Lidar (MARL) from Alfred Wegener Institute, and the TMF-Aerosol-Lidar (TAL) from Jet Propulsion Laboratory. Four in-situ backscatter sondes from University of Wyoming were successfully launched. During the campaign a total of 414 hours of lidar data were acquired. The majority of the lidar observations were performed concurrently.

Altitude profiles of backscatter ratio of the stratospheric background aerosol layer at altitudes between 15 and 25 km and of high-altitude cirrus clouds at altitudes below 13 km are analyzed and discussed. Cirrus clouds were present on 16 of the 26 campaign nights. The vertical extent and structure of optically thin cirrus layers were studied with high temporal and spatial resolution. From auto-correlation functions of backscatter ratio profiles clouds length scales of 562 m vertically and 20.6 min horizontally are derived. The wavelength dependence of aerosol depolarization is compared to T-matrix calculations.

On the basis of a sulfuric acid aerosol model, color ratio profiles obtained from two wavelength lidar data are compared to the corresponding profiles derived from the sonde observations. We find good to excellent agreement between the in-situ observations and AT-lidar and MARL data with respect to backscatter and color ratio. Comparison of measured aerosol backscatter coefficients with model results are consistent with a lognormal particle size distribution with total number density $N = 10 \text{ cm}^{-3}$, median radius $r_g = 0.075 \text{ } \mu\text{m}$, and geometric standard deviation $\sigma_g = 1.86$ below an altitude of about 19 km.

Comparisons between temperature profiles obtained by the sondes and the corresponding NCEP (National Center for Environmental Prediction) data reveal

differences of up to 6 K. In particular, NCEP temperatures are generally lower at tropopause altitudes. Also, we find that NCEP data yield tropopause altitudes several hundred meters too low in comparison with in-situ observations. Density profiles calculated from pressure and temperature data obtained during the backscatter sonde soundings deviate from the corresponding NCEP daily density profile by more than 3% in the troposphere and more than 2% in the stratosphere.

1. Introduction

During February–March 1997 an aerosol measurement campaign was carried out at Table Mountain in southern California (34.4°N, 117.7°E, 2280 m asl). Three aerosol lidar instruments participated in the campaign and four balloon-borne backscatter sondes were launched to provide independent data on the aerosol backscatter coefficient. Additionally, two of the three lidar systems and the backscatter sonde measured altitude profiles of volume depolarization at one or two wavelengths.

The objectives of the campaign were twofold. First, ground-based lidar observations of the stratosphere are an integral part of the Network for the Detection of Stratospheric Change (NDSC) where they provide information on trace gas concentrations, temperature and aerosol content. The high quality level of the NDSC data set is guaranteed by periodic intercomparisons between instruments [e.g., *McDermid et al.*, 1995; *Singh et al.*, 1996; *Steinbrecht et al.*, 1998]. Results from the individual instruments were compared in order to improve our understanding of systematic and statistical error sources in the lidar data set. Differences noted between the sonde observation of temperature, density and tropopause height could have implications for lidar (and other instruments) analyses that use the NCEP data for normalization and for the computation of Rayleigh extinction parameters. Second, the measurements enhance the data set on sub-tropical/mid-latitude high-altitude cirrus clouds. The multiwavelength polarization detection method allows for the characterization of cirrus ice particles with high temporal and spatial resolution. The measurements also provide information on the present state of stratospheric background aerosol (SBA) layer almost six years after the volcanic eruption of Mt. Pinatubo in 1991.

The paper is divided in three sections. First a brief overview over the measuring instruments is given. The data analysis is described schematically and results from individual instruments are presented. The second part is devoted to the stratospheric measurements. Lidar and sonde measurements are compared and the results are

discussed. Finally, the cirrus cloud observations are analyzed and compared to results of T-matrix scattering calculations.

2. Instruments

Three aerosol lidars participated in the campaign:

- the mobile aerosol Raman lidar (AT-lidar) from NASA Goddard Space Flight Center (GSFC), USA,
- the mobile aerosol Raman lidar (MARL) from Alfred Wegener Institute (AWI), Germany, and
- the aerosol lidar (TAL) from Jet Propulsion Laboratory (JPL) / Table Mountain Facility, USA.

In addition, four balloon-borne backscatter sondes from University of Wyoming were flown during the campaign.

2.1. AT-lidar

Table 1.

Key instrument parameters of AT-lidar are summarized in Table 1.

2.2. MARL

Table 2.

The MARL lidar employs a Nd:YAG laser as light source. The second (532 nm) and third (355 nm) harmonic of the 1064 nm fundamental wavelength are transmitted simultaneously with a pulse repetition frequency of 30 Hz. Both, elastically backscattered light from molecular and aerosol scattering and that from inelastic vibrational Raman scattering by molecular nitrogen is detected for height ranges between 5 and 30 km. Additionally, the instrument includes detection channels for cross-polarized return signals at 355 and 532 nm. The instrument operates during nighttime only.

A polychromator module separates the different wavelengths and splits the elastic signals (parallel channel) into high sensitivity (far field) and low sensitivity (near field) channels. The high sensitivity channels incorporate a mechanical chopper with a cut-off altitude of about 25 km.

Signal intensity in the eight channels is measured by sensitive, low-noise photomultipliers. Photomultiplier counts are processed by multichannel scalars. In addition, the output of three channels ([532 nm || near], [355 nm || near], [532 nm ⊥]) is recorded in analog mode using 20 MHz transient recorders. The telescope and polychromator, as well as the polychromator and photomultipliers, are connected by fiber optic cables. All the lidar instrumentation is mounted on a removable carrier inside a standard 20-ft-container. Further technical details can be found in *Schäfer et al.* [1995, 1997].

During the campaign, data were acquired for 2000 pulse (1.1 minutes) integration periods. For the following analysis, data acquired in the “far” channels were not used.

2.3. TAL

Table 3.

Like MARL and AT-lidar, TAL uses a Nd:YAG laser as light source. Using frequency doubling and tripling laser pulses at wavelengths of 355, 532 and 1064 nm are transmitted simultaneously with a pulse repetition frequency of 10 Hz. The backscattered light is collected by a Newtonian telescope. Dichroic mirrors separate the wavelengths 1064, 355, 387, and 532 nm. The parallel and perpendicular polarized components of 532 nm are obtained by a combination of a beam splitter (quartz plate) and two sheet polarizers.

Interference filters suppress sky background and increase the signal-to-noise ratio (SNR). With one exception photomultipliers operate in photon counting mode; at [532 nm ||] a Hamamatsu H5783P-06 metal package detector is used. Signals are preamplified ([532 nm ||] only) and discriminated. Signal detection is performed with

five multichannel scaler (MCS) PC plug-in boards with 2 μ sec dwell time (corresponding to an altitude resolution of 300 m) and 1024 bins signal length (corresponding to a 0–300 km range).

During data acquisition the MCS sum the count rates over a period of 1 minute (corresponding to 600 laser pulses). Each one-minute-profile is stored on hard disk. Additionally, sums over 30 or 60 minutes are performed and stored separately.

2.4. Backscatter sonde

Table 4.

The aerosol backscatter sonde is a balloon-borne instrument for the in-situ observation of stratospheric aerosols [*Rosen and Kjome*, 1991]. The instrument measures the light backscattered at a distribution of angles peaking at 173° at two wavelengths ranges centered at 490 and 940 nm, respectively. The transmitted light signal is a 7 J light pulse produced by a xenon flashlamp every 7–8 seconds. The sonde observes an air volume of about 1 m³ within a few meters distance. At an average rise velocity of about 4–5 m/s the altitude resolution is 25–35 m.

The backscattered light is measured by two photodiode detectors. Glass filters with a full width half maximum (FWHM) of approximately 150 nm centered at wavelengths of 490 and 940 nm, respectively, allow the determination of backscatter ratio at these two wavelengths. The pulse to pulse variation of the flashlamp (about 1.5% pulse-to-pulse, about 10% during one sounding) is monitored and corrected for in each channel. At 20 km altitude SNR is about 100.

The sonde includes additional sensors for measurement of ambient air temperature, air pressure, ozone partial pressure, and relative humidity. For further technical details we refer to *Rosen and Kjome* [1991].

3. Data analysis

The analysis of MARL and TAL data was performed at Table Mountain Facility (TMF) using the same data analysis program. AT-lidar and backscatter sonde data were analyzed at GSFC and University of Wyoming, respectively. Before the data analysis algorithm is described we define several quantities used in the following discussion.

The backscatter coefficient for aerosol and molecular scattering at geometrical altitude z (above sea level) and wavelength λ is denoted by $\beta^A(z, \lambda)$ and $\beta^M(z, \lambda)$, respectively. The corresponding extinction coefficients are $\alpha^A(z, \lambda)$ and $\alpha^M(z, \lambda)$, respectively. Furthermore, $\beta = \beta^A + \beta^M$ and $\alpha = \alpha^A + \alpha^M$ are the (total) backscatter and extinction coefficient, respectively.

The backscatter ratio R is defined by

$$R = \frac{\beta^M + \beta^A}{\beta^M}. \quad (1)$$

$R - 1$ is known as the aerosol backscatter ratio. Polarization lidars detect the parallel (subscript \parallel) and perpendicular (subscript \perp) polarized components of the backscattered light. Here, \parallel and \perp refer to the aligned- and cross-polarized components with respect to the plane of polarization of the transmitted (linearly polarized) beam, respectively.

The parallel backscatter ratio is defined as

$$R_{\parallel} = \frac{\beta_{\parallel}^M + \beta_{\parallel}^A}{\beta_{\parallel}^M}. \quad (2)$$

Volume depolarization δ and aerosol depolarization δ^A are defined by

$$\delta = \frac{\beta_{\perp}^M + \beta_{\perp}^A}{\beta_{\parallel}^M + \beta_{\parallel}^A} = \frac{\beta_{\perp}}{\beta_{\parallel}} \quad \delta^A = \frac{\beta_{\perp}^A}{\beta_{\parallel}^A} = \frac{\delta - \delta^M}{R_{\parallel} - 1} + \delta. \quad (3)$$

Volume depolarization of molecular scattering is $\delta^M = \beta_{\perp}^M / \beta_{\parallel}^M$. Depending on interference filter width in the receiver channel the value of δ^M varies between 0.0035 and 0.0141 [Young, 1980]. The relation between R , R_{\parallel} , and δ is

$$R = \frac{1 + \delta}{1 + \delta^M} R_{\parallel}. \quad (4)$$

We express the wavelength dependence of the aerosol backscatter coefficient in terms of the color ratio

$$C_{\lambda_1, \lambda_2} = \frac{R(\lambda_1) - 1}{R(\lambda_2) - 1} = \frac{\beta^A(\lambda_1)}{\beta^A(\lambda_2)} \left(\frac{\lambda_2}{\lambda_1} \right)^k. \quad (5)$$

Here, $k = -4.13$ denotes the wavelength dependence of molecular scattering [Ciddor, 1996].

The ratio of aerosol extinction and backscatter coefficient

$$L(z) = \frac{\alpha^A(z)}{\beta^A(z)} \quad (6)$$

is also known as lidar ratio. Correspondingly, the ratio of optical depth

$$\tau_\alpha(z_l, z_t) = \int_{z_l}^{z_t} dz \alpha^A(z) \quad (7)$$

and column backscatter coefficient

$$\tau_\beta(z_l, z_t) = \int_{z_l}^{z_t} dz \beta^A(z) \quad (8)$$

gives the column lidar ratio

$$L_c(z_l, z_t) = \frac{\tau_\alpha(z_l, z_t)}{\tau_\beta(z_l, z_t)}. \quad (9)$$

3.1. MARL and TAL

The analysis of the MARL and TAL data was performed in three steps. First, the raw signal count rates of each channel were averaged over time periods ranging from 1 minute to 60 minutes. The following analysis procedure was applied to each of the averaged data sets. Second, the averaged raw signals were corrected for photodetector saturation, deadtime effects, background noise, signal induced noise (SIN), and cross-talk between and s- and p-polarization channels. Finally, the backscatter ratio and backscatter coefficients were calculated using Klett's method [Klett, 1981, 1985]. The extinction-to-backscatter-ratio was taken to be 30 and 40 sr above 14 km altitude at 355

and 532 nm, respectively. Below 14 km cirrus cloud particles were frequently observed and $L^A(z, \lambda) = 30$ sr was assumed, independent of λ . The molecular backscatter coefficient was calculated from a number density profile

$$\beta^M(z, \lambda) = \frac{d\sigma}{d\Omega}(\lambda) \mathcal{N}(z) \quad \text{where} \quad \mathcal{N}(z) = \frac{p(z)}{kT(z)}. \quad (10)$$

Daily temperature and pressure profiles, $T(z)$ and $p(z)$, were obtained from the NCEP data base.

By comparing number density profiles derived from NCEP data with the corresponding profile derived from in-situ temperature and pressure profiles we found significant deviations on the order of more than 3%, mainly in the tropopause region. In the stratosphere deviations of more than 2% occurred. We note that an error in the density profile of 2% translates to first approximation in an error of the aerosol backscatter ratio of the same magnitude.

If Raman signals were available a method for the determination of R due to *Ansmann et al.* [1992] was used as well. The Raman backscatter ratio was derived from the corrected elastic and inelastic return signals, $P_{||}(z, \lambda)$ (or $P(z, \lambda)$) and $P(z, \lambda^R)$, by

$$\begin{aligned} R_{||}(z) &= K_1 \frac{P_{||}(z, \lambda)}{P(z, \lambda^R)} \exp \int_{z_s}^z d\tilde{z} \left(\alpha^M(\tilde{z}, \lambda) - \alpha^M(\tilde{z}, \lambda^R) \right) \\ R(z) &= K_2 \frac{P(z, \lambda)}{P(z, \lambda^R)} \exp \int_{z_s}^z d\tilde{z} \left(\alpha^M(\tilde{z}, \lambda) - \alpha^M(\tilde{z}, \lambda^R) \right). \end{aligned} \quad (11)$$

Here, $\lambda^R = (\lambda^{-1} - 2329.66 \text{ cm}^{-1})^{-1}$ denotes the N_2 Raman shifted wavelength and z_s is the altitude of the lidar instrument. The constant K_1 (K_2) was determined by normalizing $R_{||}$ (R) to unity between 14 and 16 km since no cirrus cloud layers were observed above 14 km during the campaign.

Volume depolarization δ was calculated by forming the ratio of the photon counts in the aligned- and cross-polarized detection channels,

$$\delta(z, \lambda) = K \frac{P_{\perp}(z, \lambda)}{P_{||}(z, \lambda)}. \quad (12)$$

The constant K follows from normalization of δ to δ^M at an aerosol-free altitude range between 14 and 20 km.

The value of δ^M changes depending whether the rotational Raman lines are included [Young, 1982]. That is, δ^M is a function of the FWHM of the filter transmission curve. In general, δ^M is given by

$$\delta^M = \frac{3\epsilon x_C + 9\epsilon x_R}{180 + 4\epsilon x_C + 12\epsilon x_R}. \quad (13)$$

Here, $\epsilon = 0.2163$ and x_C and x_R denote the relative intensity weighted by the transmission curve of the interference filter

$$x_C = \mathcal{T}(\lambda^C) \quad x_R = \frac{\sum_i \mathcal{T}(\lambda_i^R) I(\lambda_i^R)}{\sum_i I(\lambda_i^R)}. \quad (14)$$

$\mathcal{T}(\lambda)$ denotes filter transmission at wavelength λ , λ^C the central Cabannes wavelength. $I(\lambda^R)$ is the relative intensity of a rotational Raman line at wavelength λ^R , and the sum runs over all rotational Raman lines. If the transmission curve includes the rotational Raman lines without attenuation relative to the Cabannes line, $x_R = x_C$ and $\delta^M = 0.0141$. On the other hand, if the rotational Raman lines are blocked completely ($x_R = 0$) only the Cabannes line contributes and $\delta^M = 0.0035$ is obtained. For the filter FWHM used by MARL and TAL we obtained $\delta^M = 0.0136$ and $\delta^M = 0.0045$, respectively.

In order to compensate cross-talk between s- and p-detection channel a 2% cross-talk correction has been applied to the TAL data.

3.2. Backscatter sonde

The basic backscatter data is a peak voltage level measured and recorded after each triggering of the flash tube. In the analysis, the backscatter ratio was determined by dividing the measured peak value by the calculated peak voltage for aerosol free air at the ambient pressure and temperature. The response of the instrument at ground

level pressure and temperature conditions was determined through calibration with an ensemble of 4 standard backscatter sondes maintained at Laramie, or by direct measurement in a clean air tower.

For the low aerosol conditions encountered during the flights it was necessary to identify any sensitivity drift (as could be induced by the extreme environmental temperature and pressure conditions) and make necessary corrections if needed. Any drift was easily detected by comparison of ascent and descent data.

For low aerosol conditions, sources of errors and uncertainties need to be considered. The repeatability of any given calibration is about 1%. In addition, a typical 2% drift in calibration may occur during shipment of the sonde. However, in this case the sondes were personally escorted and probably did not experience a sudden change in calibration due to mishandling. If corrections to drift are necessary, this could lead to an additional uncertainty of 1 or 2%. There is a small residual signal from light scattered by parts of the instrument package back into the photometers. For the altitudes of interest here this effect was about 1% or less. The absolute calibration was thought to be accurate to 1 or 2%. Thus, the typical root-mean-square uncertainty in a typical sounding may be 2 to 3%. Certainly, $\pm 2\%$ is the best that could reasonably be expected from the backscatter sonde. Unfortunately, even such a small uncertainty can lead to a relatively large uncertainty for low aerosol conditions. For example, if the backscatter ratio is 1.08, the aerosol backscatter ratio would be 0.08 and the 2% uncertainty suggested above now translates to a 25% uncertainty in the aerosol backscatter ratio.

4. Measurement results and discussion

The lidar measurements took place between 19 February and 18 March 1997 at the Table Mountain Facility / Jet Propulsion Laboratory in southern California (34.4°N, 117.7°E, 2280 m asl). The three aerosol lidar systems were placed in close proximity. The distance between MARL and TAL was about 30 m and the AT-lidar was about

300 m farther away. Tests showed that all three aerosol lidars could be operated simultaneously with no detectable interference or cross-talk between the instruments. During the campaign a total of 413.6 hours of lidar data were acquired. An overview of the daily measurement periods during the campaign is given in Table 5. On 16 of 26 nights cirrus clouds could be observed in the upper troposphere. In the lower stratosphere AT-lidar, MARL, and the backscatter sonde results data show the presence of the stratospheric background aerosol layer. Scattering ratios obtained by TAL in this altitude region were too small for statistically meaningful results.

Table 5.

4.1. Stratospheric background aerosol

The stratospheric background aerosol (SBA) layer consists of sub-micron sized droplets of a liquid $\text{H}_2\text{SO}_4/\text{H}_2\text{O}$ solution [Hamill *et al.*, 1997]. At mid-latitudes this aerosol layer ("Junge layer") is found at altitudes between 15 and 25 km [Junge and Manson, 1961; Junge *et al.*, 1961]. Pinnick *et al.* [1976] give a parameterization of the size distribution of the stratospheric background aerosol in terms of a lognormal distribution

$$\frac{dN}{dr} = \frac{N_0}{\sqrt{2\pi} r \ln \sigma_g} \exp \left(-\frac{\ln^2(r/r_m)}{2 \ln^2 \sigma_g} \right), \quad (15)$$

where $N_0 = 10 \text{ cm}^{-3}$, $r_m = 0.075 \text{ } \mu\text{m}$, and $\sigma_g = 1.86$ denote the particle number density, the median radius, and the geometric standard deviation, respectively [Pinnick *et al.*, 1976].

The lidar and in-situ instruments measured intensities of backscattered light at several different wavelengths: 532 nm (AT-lidar, and MARL), 351/355 nm (AT-lidar only), and 490/940 nm (backscatter sonde). Since the aerosol backscatter and extinction coefficients are wavelength dependent the comparison was performed on the basis of a simple aerosol model which tied the two data sets together. The model is based on the assumption that the SBA consists of $\text{H}_2\text{SO}_4/\text{H}_2\text{O}$ droplets in equilibrium with 5 ppmv

ambient water vapor mixing ratio [Hamill *et al.*, 1997; Steele and Hamill, 1981]. With a known droplet composition, the refractive index m as a function of wavelength and altitude can be calculated [Palmer and Williams, 1975]. For the wavelengths considered here the imaginary part of m is negligible. The refractive indices increase slightly with altitude as decreasing temperatures lead to higher sulfuric acid concentrations. The aerosol backscatter and extinction coefficients then follow from Mie calculations

$$\begin{aligned}\beta^A(\lambda) &= \int_0^\infty dr \frac{dN}{dr} \pi r^2 Q_b\left(\frac{2\pi r}{\lambda}, m\right) \\ \alpha^A(\lambda) &= \int_0^\infty dr \frac{dN}{dr} \pi r^2 Q_e\left(\frac{2\pi r}{\lambda}, m\right).\end{aligned}\quad (16)$$

$Q_b(2\pi r/\lambda, m)$ and $Q_e(2\pi r/\lambda, m)$ denote the Mie backscatter and extinction efficiency, respectively, for spherical particle of radius r and refractive index m at wavelength λ [Bohren and Huffman, 1983]. The size distribution dN/dr is given by Equation 15. Furthermore, the size distribution parameters N_0 , r_m , and σ_g were assumed to be constant throughout the aerosol layer.

The model predicts values of color ratios $C_{532/355}$ and $C_{940/490}$ (Eqn. 5) for the wavelength pairs 532/355 nm and 940/490 nm, respectively,

$$C_{532/355} \approx 2.40 \quad C_{940/490} \approx 5.56. \quad (17)$$

Due to the altitude dependence of m the actual values of C vary by about 1% between 20 and 25 km.

Figure 1.

The AT-lidar and MARL backscatter ratio profiles indicating the presence of SBA are shown in Figure 1. The right panel gives the results from the sonde observations at 490 nm on 11 and 13 March 1997, the left panel the corresponding AT-lidar profiles at 532 nm on the same days. Due to lower SNRs the MARL data had to be averaged over the whole measurement period in order to obtain the profile shown in the middle panel. Averaging over a time period of several weeks can be justified as the AT-lidar data set shows very little temporal variation of the SBA layer (see Figure 2).

Figure 2.

Also shown in Figure 1, as thick vertical lines, is the backscatter ratio derived from the Mie calculations. The good to excellent agreement between observation and model at altitudes between about 15 to 19 km suggests that the in-situ and the lidar results are in agreement within the error bars of the measurement. Model results and observations in Figure 1 differ considerably above 19 km. At those higher altitudes the parameterization of N_0 , r_m , and σ_g is no longer valid.

Figure 3.

The color ratio profile for the 532/355 nm lidar channels and the corresponding profile for the 940/490 nm wavelength pair of the in-situ sonde is shown in Figure 3. Thick lines indicate the model result. At almost all altitude levels between 15 and 25 km model result and observations agree at the 2-sigma-level. Since color ratio does not depend on particle number density N_0 the agreement between model and observation with respect to color ratio (Figure 3) and the disagreement with respect to backscatter ratio (Figure 1) suggest that the true value of N_0 during the campaign was less than 10 cm^{-3} above about 20 km.

4.2. High-altitude cirrus

During the campaign high-altitude cirrus clouds were frequently observed. On 16 of the total of 26 measurement nights backscatter and volume depolarization profiles indicated the presence of cirrus layers (cf. Table 5).

Figure 4.

In general, the observed cirrus exhibited a high degree of variability, both vertically and horizontally. For example, during the first BKS sonde flight the backscatter ratio profiles at 490 and 940 nm reveal two distinct layers separated by less than 300 m. The over-all vertical extent of the clouds was on the order of 500 m. The measured color ratio (right panel) suggests that the top layer consisted mainly of particles with dimensions much larger than the BKS wavelengths as in this case $\beta^A(\lambda) \approx \text{const}$ and thus $C_{940/490} \approx (490, \text{nm}/940, \text{nm})^{-4.13} = 14.7$.

Figure 5.

The three lidars were operated concurrently during the sonde flights. However, the

horizontal drift of the BKS instruments precludes a direct intercomparison of sonde and lidar data. The high vertical resolution of the sonde profiles is complemented by the enhanced temporal resolution of the lidar profiles. As an example for the lidar measurements Figure 5 shows the observations of backscatter ratio (middle) and volume depolarization (bottom) at 532 nm by TAL of 13 March 1997. The marks above the figure indicate the measurement times of the individual profiles (one profile per minute). During the first half of the measurement a strongly depolarizing layer at altitudes between 10 and 12 km was observed. This layer descended downwards to 8–9 km during the night. During the second half of the measurement a low-depolarization subvisual cloud appeared at the tropopause.

Figure 6.

In the top panel of Figure 5 the aerosol backscatter coefficient integrated between 9 and 14 km is plotted. The dotted line marks the subvisibility threshold of 10^{-3} sr^{-1} . This value is derived from an optical depth subvisibility threshold of $\tau = 0.03$ at 532 nm [Sassen *et al.*, 1989] in the following way.

Optical depth at 532 nm was calculated from MARL Raman signals at 607 nm [Beyerle *et al.*, 1998]. By comparison of optical depth with the altitude integrated aerosol backscatter coefficient we obtain a average column lidar ratio at 532 nm of 30 sr with an estimated uncertainty of at least 50%. The subvisibility threshold in terms of the aerosol backscatter column is thus about $0.03 / 30 \text{ sr} = 10^{-3} \text{ sr}^{-1}$. Figure 6 shows the relation between integrated aerosol backscatter coefficient and optical depth. The dotted lines indicate column lidar ratios of 45 and 30 sr^{-1} , respectively.

Figure 5 illustrates several features typical for the cirrus observations throughout the campaign. First, the cirrus layers were highly structured on length scales of several hundreds of meters vertically and several minutes horizontally. Second, frequently the cirrus layers were observed in close proximity to the temperature tropopause. During the campaign no clouds were found in the lower stratosphere. Third, subvisible cirrus clouds with integrated backscatter coefficients below 10^{-3} sr^{-1} or optical depth below

0.03 occurred regularly. Furthermore, depolarization data suggest that depolarizing (non-spherical) particles and non-depolarizing (spherical and/or small) particles co-existed within several hundreds of meters.

Figure 7.

In order to quantify the vertical and horizontal (temporal) variability we use the auto-correlation function $A_v(z, t)$ and $A_h(z, t)$ of backscatter ratio $R(z, t)$ at 532 nm based on 95 h of TAL cirrus observations,

$$\begin{aligned} A_v(z_j, t_k) &= \frac{1}{j+1} \sum_{i=0}^j \left(R(z_{M-(j-i)}, t_k) - 1 \right) \cdot \left(R(z_{j-i}, t_k) - 1 \right) \\ A_h(z_j, t_k) &= \frac{1}{k+1} \sum_{i=0}^k \left(R(z_j, t_{N-(k-i)}) - 1 \right) \cdot \left(R(z_j, t_{k-i}) - 1 \right). \end{aligned} \quad (18)$$

M and N denote the number of measurements in vertical and temporal direction, respectively. As an estimate of the typical horizontal and vertical length scales of the observed cirrus clouds we take the FWHM of $A_v(z, t)$ and $A_h(z, t)$. For 15 TAL measurements—each containing between 225 and 540 individual profiles— $A_v(z, t)$ and $A_h(z, t)$ were calculated. The average over the auto-correlation functions are plotted in Figure 7. The FWHMs are 562 m and 20.6 min, respectively.

Figure 8.

Cirrus layers were frequently found in close vicinity to or below the tropopause (cf. Figure 5). For the data analysis the tropopause altitudes were derived from daily NCEP temperature profiles. However, the tropopause altitudes derived from the four BKS flights were between 250 and 590 m higher than the corresponding NCEP values. Figure 8 shows the NCEP tropopause altitudes together with four altitude values calculated from the in-situ profiles. Taking into account an offset between NCEP and true tropopause altitude on the order of several hundreds of meters the observations are suggest that during the campaign no clouds occurred above the temperature tropopause.

Figure 9.

The analysis of histogram functions shown in Figure 9 provides information on the occurrence probability of visual and subvisual cirrus clouds. The distribution function of the altitude integrated backscatter coefficient at 532 nm is given in Figure 9. The integration was performed between $z_i = 9$ km and $z_t = 14$ km. Based on 8748 individual

profiles observed by TAL we find that 1369 profiles (15.6%) indicated the presence of optical thick clouds with $\tau_\beta > 10^{-3} \text{ sr}^{-1}$. 1571 (18.0%) yield column backscatter coefficients between the instrument detection limit of $2 \cdot 10^{-4} \text{ sr}^{-1}$ and 10^{-3} sr^{-1} . In comparison, *Beyerle et al.* [1998] derived occurrence distributions for tropical cirrus clouds during October/November of 30.1% for visible 42.3% for subvisible clouds. However, these percentages are based on only 57 h of data.

In Figure 10 the parallel color ratio

$$C_{\parallel} = \frac{R_{\parallel}(\lambda_1) - 1}{R_{\parallel}(\lambda_2) - 1} = \frac{\beta_{\parallel}^A(\lambda_1)}{\beta_{\parallel}^A(\lambda_2)} \left(\frac{\lambda_2}{\lambda_1} \right)^k \quad (19)$$

is plotted against the perpendicular color ratio

$$C_{\perp} = C_{\parallel} \frac{\delta^A(\lambda_1)}{\delta^A(\lambda_2)} = \frac{\beta_{\perp}^A(\lambda_1)}{\beta_{\perp}^A(\lambda_2)} \left(\frac{\lambda_2}{\lambda_1} \right)^k. \quad (20)$$

as calculated from the MARL 532 nm profiles. At four temperature ranges between 210 and 230 K a cluster of data points centered at $C_{\perp} \approx 1$ and $C_{\parallel} \approx 1$ appears. Typically, these events show low backscatter ratios close to unity. At large values of R data points are distributed along $C_{\parallel} \approx 0.2$ with C_{\perp} varying by more than order of magnitude. We identify the two clusters as the “small particle” and “large particle” regions. If particle dimensions are much smaller than the wavelength $\beta^A(\lambda) \propto \lambda^k$ (cf. Eqn. 5) and $C_{\parallel} \approx 1$. Similarly, if particle dimension are much larger than the wavelength the geometric optics approximation is valid and $\beta^A(\lambda) \propto \text{const.}$ Thus, $C_{\parallel} \approx (532/355)^k = 0.2$. We note however, that the large variation of C_{\perp} suggests that even for large particles C_{\perp} contains a significant amount of information with respect to particle shape.

In order to interpret these findings we performed T-matrix scattering calculation using computer source code developed by Michael Mishchenko at the NASA Goddard Institute for Space Studies, New York [*Mishchenko and Travis, 1994; Mishchenko et al., 1996*]. Due to limited computing resources we restricted our calculations to monodispers size distributions of randomly oriented spheroidal particles with equal-volume-radii

Figure 10.

Figure 11.

between 0.01 and 1 μm and aspect ratios varying between 0.5 (prolate shape) and 2.5 (oblate shape). The composition is assumed to be water ice with refractive index [Warren, 1984]

$$\begin{aligned} m(355\text{ nm}) &= 1.325 + i 3.76 \cdot 10^{-9} \\ m(532\text{ nm}) &= 1.312 + i 3.11 \cdot 10^{-9} . \end{aligned} \quad (21)$$

Figure 11 shows the result. Small particles with radii less than about 0.02 μm exhibit perpendicular and parallel color ratios close to unity. For larger radii between 0.02 μm and 0.05 μm the relation between C_{\parallel} and C_{\perp} seems to follow

$$C_{\perp} \propto (C_{\parallel})^n \quad (22)$$

with n changing with aspect ratio. For larger particles sizes no clear signature is apparent. However, we note that for $r > 0.2 \mu\text{m}$ and oblate particle shapes the variability in C_{\perp} exceeds the variability in C_{\parallel} .

From the comparison between observations and model results we draw the following conclusions. First, the cluster of observations close to $C_{\perp} \approx 1 \approx C_{\parallel}$ is consistent with the presence of sub-micron sized particles. The larger particles populate this region only for specific radii and aspect ratios. Second, the relationship between C_{\perp} and C_{\parallel} is strongly dependent on particle shape. In particular, the results for oblate spheroids (aspect ratio = 2.5) seems to correspond closest to the observations. Clearly, more detailed investigations are necessary. The model calculations should be extended to realistic size distributions and particle dimensions of at least several tens of μm should be considered.

5. Conclusions and outlook

The analysis and comparison of more than 400 h worth of aerosol lidar data and four in-situ backscatter sonde profiles lead us to the following conclusions.

- AT-lidar, MARL and BKS observations of the stratospheric background aerosol layer are in good to excellent agreement within its error bars. The Junge layer showed little variability during the measurement campaign.
- Frequently cirrus clouds were found close to the tropopause. There is no indication that cirrus cloud occur in the lower stratosphere. The observed cirrus layers exhibited a high degree of spatial inhomogeneity. The relationship between parallel and perpendicular color ratio suggests sub-micron sized particles can occur within cirrus clouds.
- Density profiles based on NCEP temperature and pressure data exhibit deviations from observations of about 3% at the tropopause and about 2% in the stratosphere.

As a result of this intercomparison campaign the MARL instrument is currently being improved and repaired. The far range detection channels will be optimized for the observations of the stratospheric background aerosol. Furthermore, a new multiwavelength aerosol lidar currently under development at Table Mountain Facility will replace the TAL instrument in the near future.

Acknowledgments. Helpful discussion with R. Neuber and M. Wirth are gratefully acknowledged. We thank M. Mishchenko from NASA Goddard Institute for Space Studies for providing computer source code used in the T-matrix scattering calculations. We gratefully acknowledge financial support for the MARL instrument by Deutsche Bundesstiftung Umwelt, Germany. GB thanks the National Research Council for the award of an associateship. The work described here was performed at the Jet Propulsion Laboratory, California Institute of Technology, through an agreement with the National Aeronautics and Space Administration. Contribution 1388 of the Alfred Wegener Institute.

References

- Ansmann, A., U. Wandinger, M. Riebesell, C. Weitkamp, and W. Michaelis, Independent measurement of extinction and backscatter profiles in cirrus clouds by using a combined Raman elastic-backscatter lidar, *Appl. Opt.*, **31**, (33), 7113–7131, 1992.
- Beyerle, G., H.-J. Schäfer, R. Neuber, O. Schrems, and I. S. McDermid, Dual wavelength lidar observation of tropical high-altitude cirrus clouds during the ALBATROSS 1996 campaign, *Geophys. Res. Lett.*, **25**, (6), 919–922, 1998.
- Bohren, C. F., and D. R. Huffman, *Absorption and scattering of light by small particles*, John Wiley & Sons, New York, 1983.
- Ciddor, P. E., Refractive index of air: new equations for the visible and near infrared, *Appl. Opt.*, **35**, (9), 1566–1573, 1996.
- Hamill, P., E. J. Jensen, P. B. Russell, and J. J. Bauman, The life-cycle of stratospheric aerosol particles, *Bull. Amer. Meteor. Soc.*, **78**, (7), 1395–1410, 1997.
- Junge, C., and J. Manson, Stratospheric aerosol studies, *J. Geophys. Res.*, **66**, (7), 2163–2182, 1961.
- Junge, C., C. Chagnon, and J. Manson, Stratospheric aerosols, *J. Meteorol.*, **18**, 81–108, 1961.
- Klett, J. D., Stable analytical inversion solution for processing lidar returns, *Appl. Opt.*, **20**, (2), 211–220, 1981.
- Klett, J. D., Lidar inversion with variable backscatter/extinction ratios, *Appl. Opt.*, **24**, (11), 1638–1643, 1985.
- McDermid, I. S., S. M. Godin, and T. D. Walsh, Results from the Jet Propulsion Laboratory stratospheric ozone lidar during STOIC 1989, *J. Geophys. Res.*, **100**, (D5), 9263–9272, 1995.
- Mishchenko, M. I., and L. D. Travis, T-matrix computations of light scattering by large spheroidal particles, *Opt. Commun.*, **109**, 16–21, 1994.
- Mishchenko, M. I., L. D. Travis, and D. W. Mackowski, T-matrix computations of light-

- scattering by nonspherical particles — A review, *J. Quant. Spectrosc. Radiat. Transfer*, **55**, (5), 535–575, 1996.
- Palmer, K. F., and D. Williams, Optical constants of sulfuric acid: Application to the clouds of Venus?, *Appl. Opt.*, **14**, (1), 208–219, 1975.
- Pinnick, R. G., J. M. Rosen, and D. J. Hofmann, Stratospheric aerosol measurements III: Optical model calculations, *J. Atmos. Sci.*, **33**, 304–314, 1976.
- Rosen, J. M., and N. T. Kjöme, Backscattersonde: A new instrument for atmospheric research, *Appl. Opt.*, **30**, (12), 1552–1561, 1991.
- Sassen, K., M. K. Griffin, and G. C. Dodd, Optical scattering and microphysical properties of subvisual cirrus clouds, and climatic implications, *J. Appl. Meteorol.*, **28**, 91–98, 1989.
- Schäfer, H.-J., O. Schrems, G. Beyerle, B. Hofer, W. Mildner, F. A. Theopold, W. Lahmann, C. Weitkamp, and M. Steinbach, A modular and mobile multi-purpose lidar system for observation of tropospheric and stratospheric aerosols, *SPIE EurOpto series*, **2581**, 128–136, 1995.
- Schäfer, H.-J., O. Schrems, G. Beyerle, B. Hofer, W. Mildner, and F. A. Theopold, Shipborne measurements with a modular multi-purpose mobile lidar system for tropospheric and stratospheric aerosol observations, *SPIE EurOpto series*, **3104**, 265–272, 1997.
- Singh, U. N., T. J. McGee, and M. R. Gross, UARS ozone and temperature validation by GSFC lidar during UARS correlative measurement campaigns (1992–1995), in *Advances in Atmospheric Remote Sensing with Lidar, Selected papers of the 18th International Laser Radar Conference (ILRC), Berlin, 22-26 July 1996*, edited by A. Ansmann, R. Neuber, P. Rairoux, and U. Wandinger, 533–536, Springer, 1996.
- Steele, H. M., and P. Hamill, Effects of temperature and humidity on the growth and optical properties of sulphuric acid-water droplets in the stratosphere, *J. Aerosol Sci.*, **12**, (6), 517–528, 1981.
- Steinbrecht, W., M. R. Gross, T. J. McGee, R. Neuber, P. v. d. Gathen, P. Wahl, U. Klein, and J. Langer, Results of the Ny-Ålesund ozone measurements intercomparison NAOMI, in

- Proceedings of the 19th International Laser Radar Conference*, edited by U. N. Singh, S. Ismail, and G. K. Schwemmer, 347-350, NASA Langley Research Center, 1998.
- Warren, S. G., Optical constants of ice from the ultraviolet to the microwave, *Appl. Opt.*, **23**, (8), 1206-1225, 1984.
- Young, A. T., Revised depolarization correction for atmospheric extinction, *Appl. Opt.*, **19**, (20), 3427-3428, 1980.
- Young, A. T., Rayleigh scattering, *Physics Today*, 42-48, January 1982.
-
- G. Beyerle, Alfred Wegener Institute for Polar and Marine Research, Postfach 600149, D-14401 Potsdam, Germany. (e-mail: gbeyerle@awi-potsdam.de)
- M. R. Gross, University of Maryland, Baltimore County, USA
- D. A. Haner, California State Polytechnic University, 3801 West Temple Avenue, Pomona CA 91768, USA
- I. S. McDermid, Table Mountain Facility, Jet Propulsion Laboratory, California Institute of Technology, P.O.Box 367, Wrightwood, CA 92397, USA
- T. J. McGee, Laboratory for Atmospheres, Code 910, Goddard Space Flight Center, Greenbelt MD 20771, USA
- J. M. Rosen and N. T. Kjome, Department of Physics & Astronomy, University of Wyoming, P.O. Box 3905 University Station Laramie, WY 82071, USA
- H.-J. Schäfer, INNOSOFT GmbH, Sachsenring 83, D-50667 Köln, Germany, Germany
- O. Schrems, Alfred Wegener Institute, Postfach 120161, D-27515 Bremerhaven, Germany

Received _____; revised _____; accepted _____.

This manuscript was prepared with AGU's \LaTeX macros v4, with the extension package 'AGU++' by P. W. Daly, version 1.5e from 1997/11/18.

Figure Captions

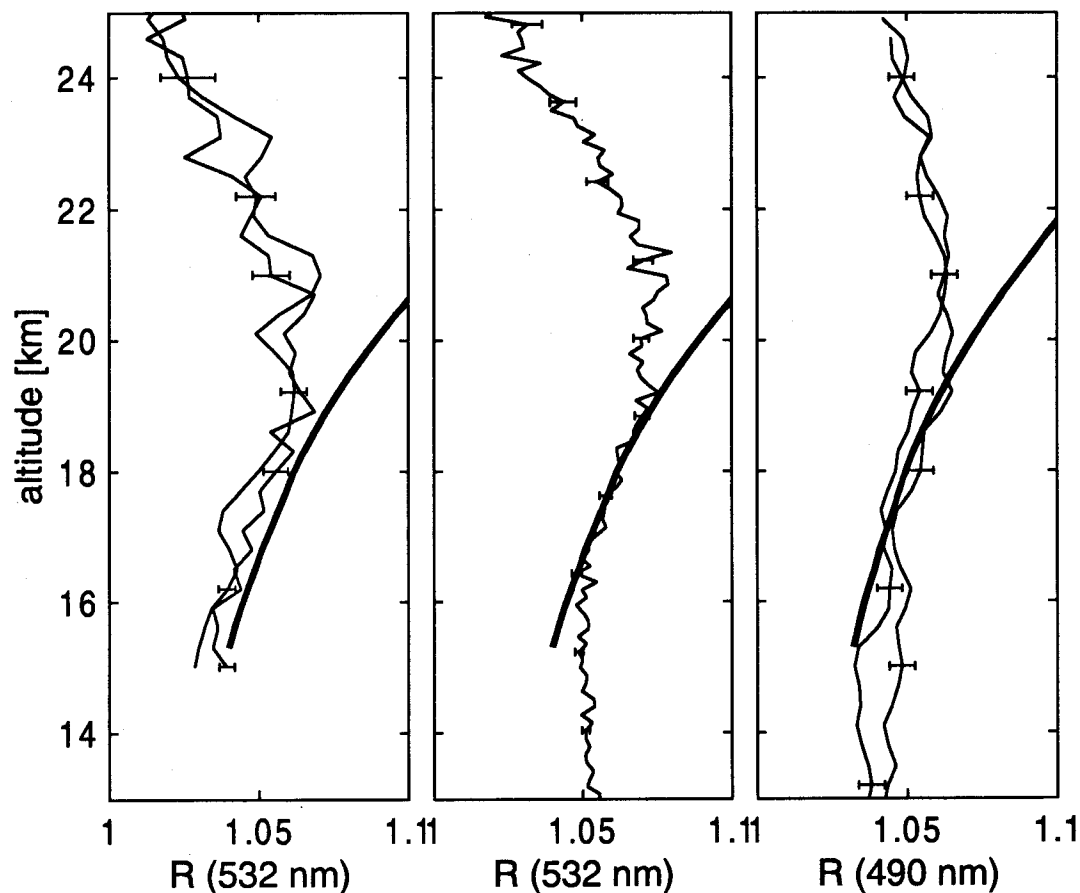


Figure 1. Stratospheric background aerosol observations of AT-lidar (left), MARL (middle), and BKS (right) in terms of the backscatter ratio at 532 nm (AT-lidar and MARL) and 490 nm (BKS). The profiles were recorded on 11 March (full lines) and 13 March 1997 (dashed lines); the MARL data is an average over the whole campaign period. The thick lines give the result obtained by the aerosol model.

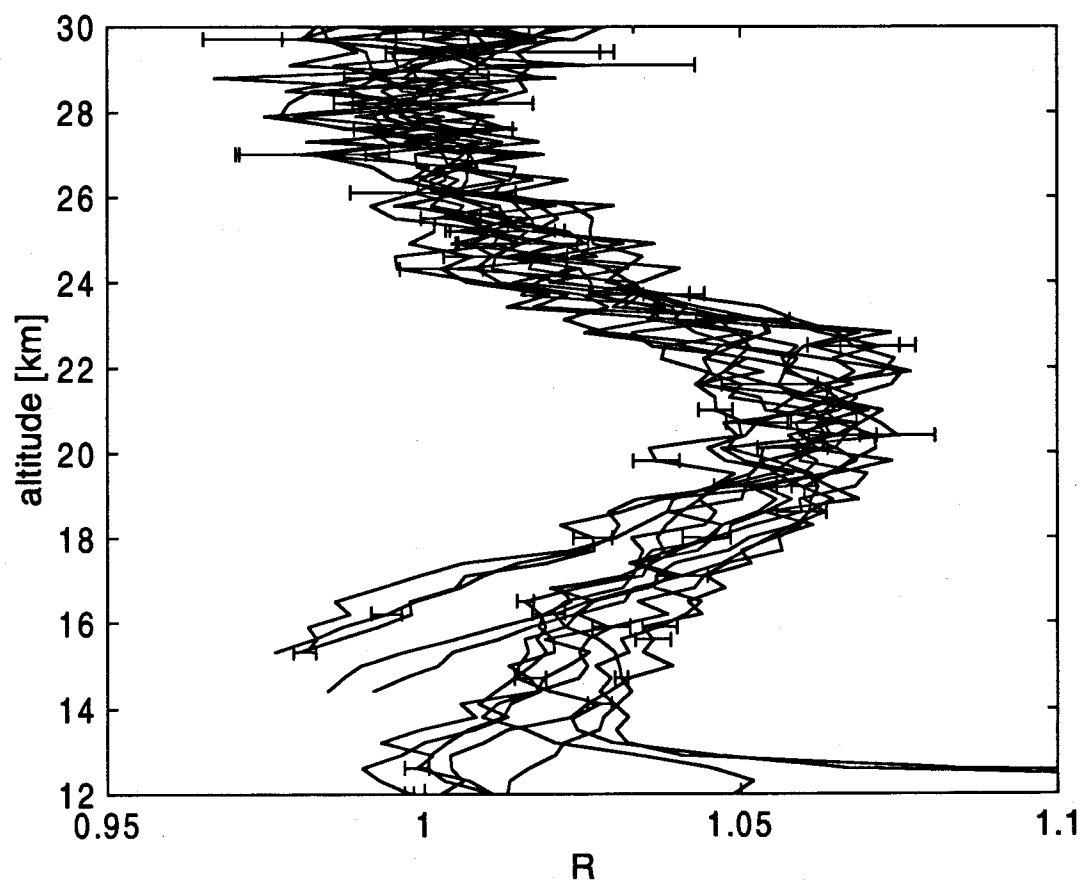


Figure 2. AT-lidar observations of the stratospheric background aerosol layer. The 13 profiles, showing backscatter ratio at 532 nm, were recorded between 2 March and 13 March 1997.

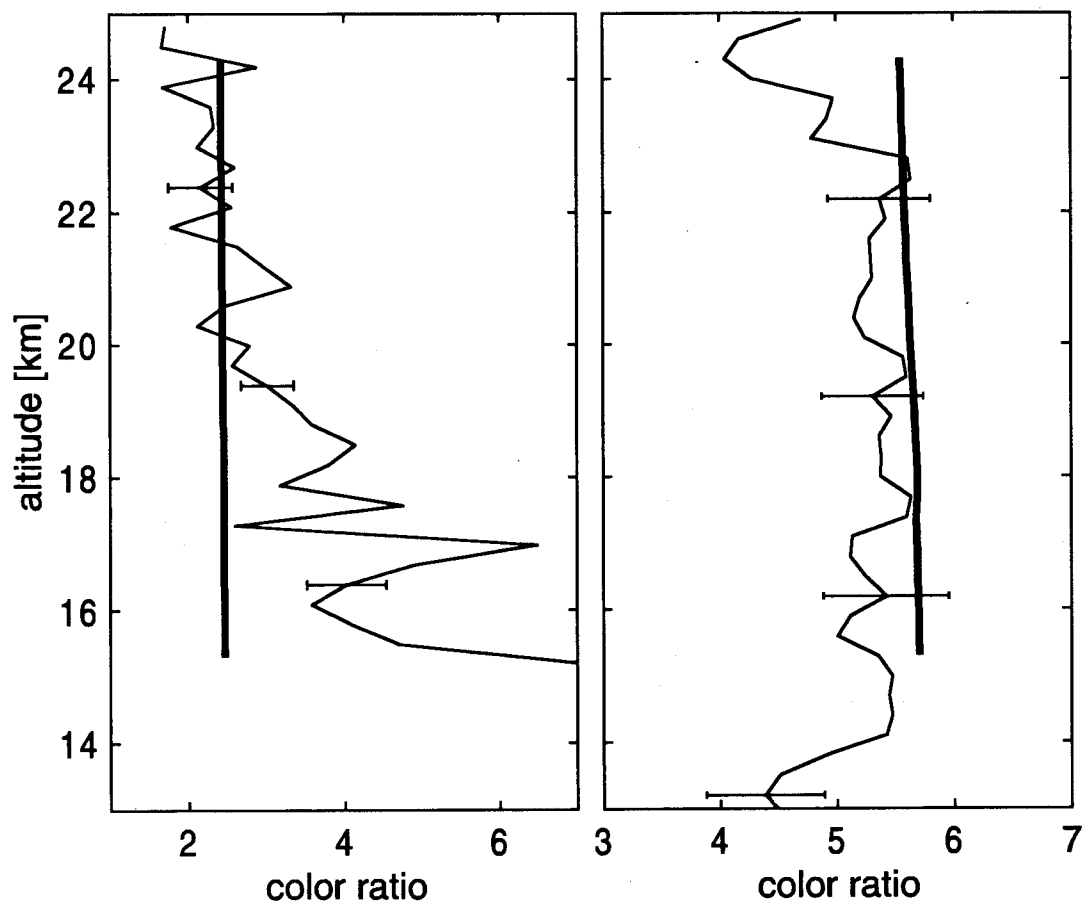


Figure 3. Color ratio at 532 nm, 351 nm (AT-lidar, left panel) and at 940 nm, 490 nm (BKS, right panel) as observed on 13 March 1997 (dashed line). The thick lines give the result obtained by the aerosol model.

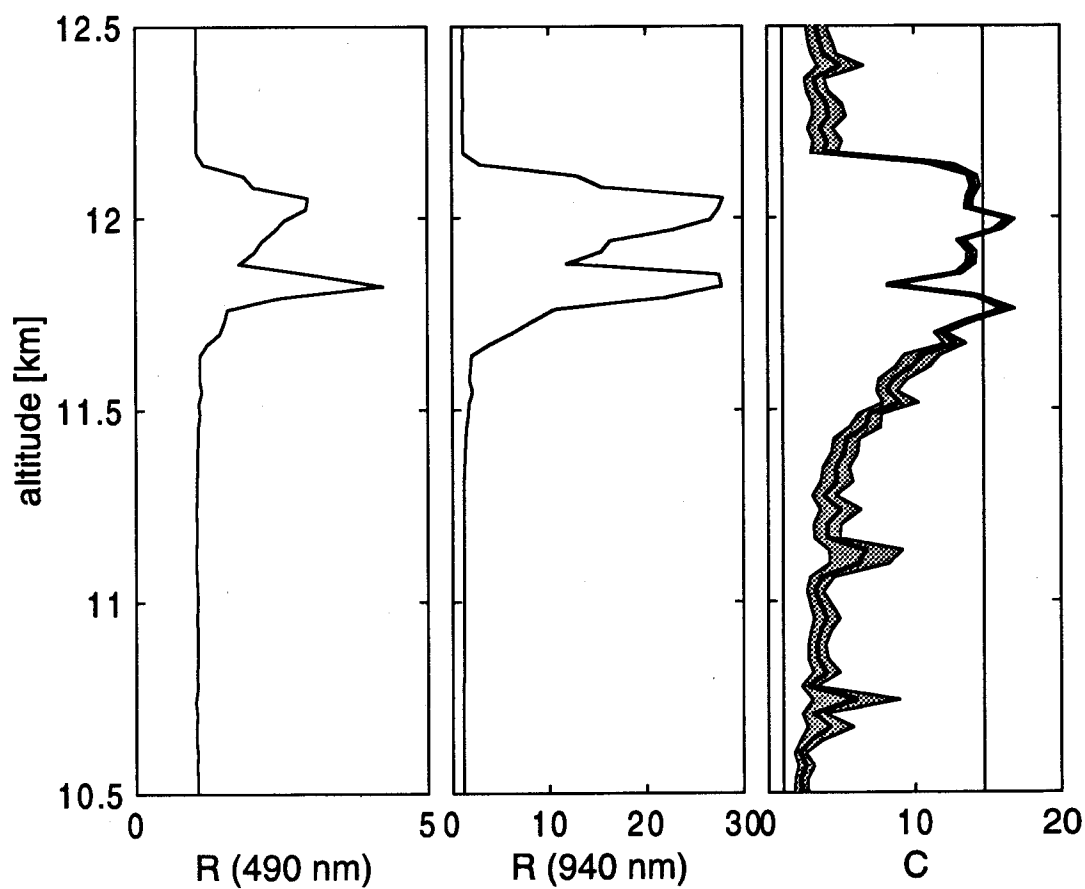


Figure 4. Backscatter ratio profiles derived from BKS flight 1 (11 March 1997) exhibit layered structures with vertical scales of a few tens of meters within the cloud layer at 490 nm (left) and 940 nm (middle). The right panel shows the corresponding color ratio profile (full line).

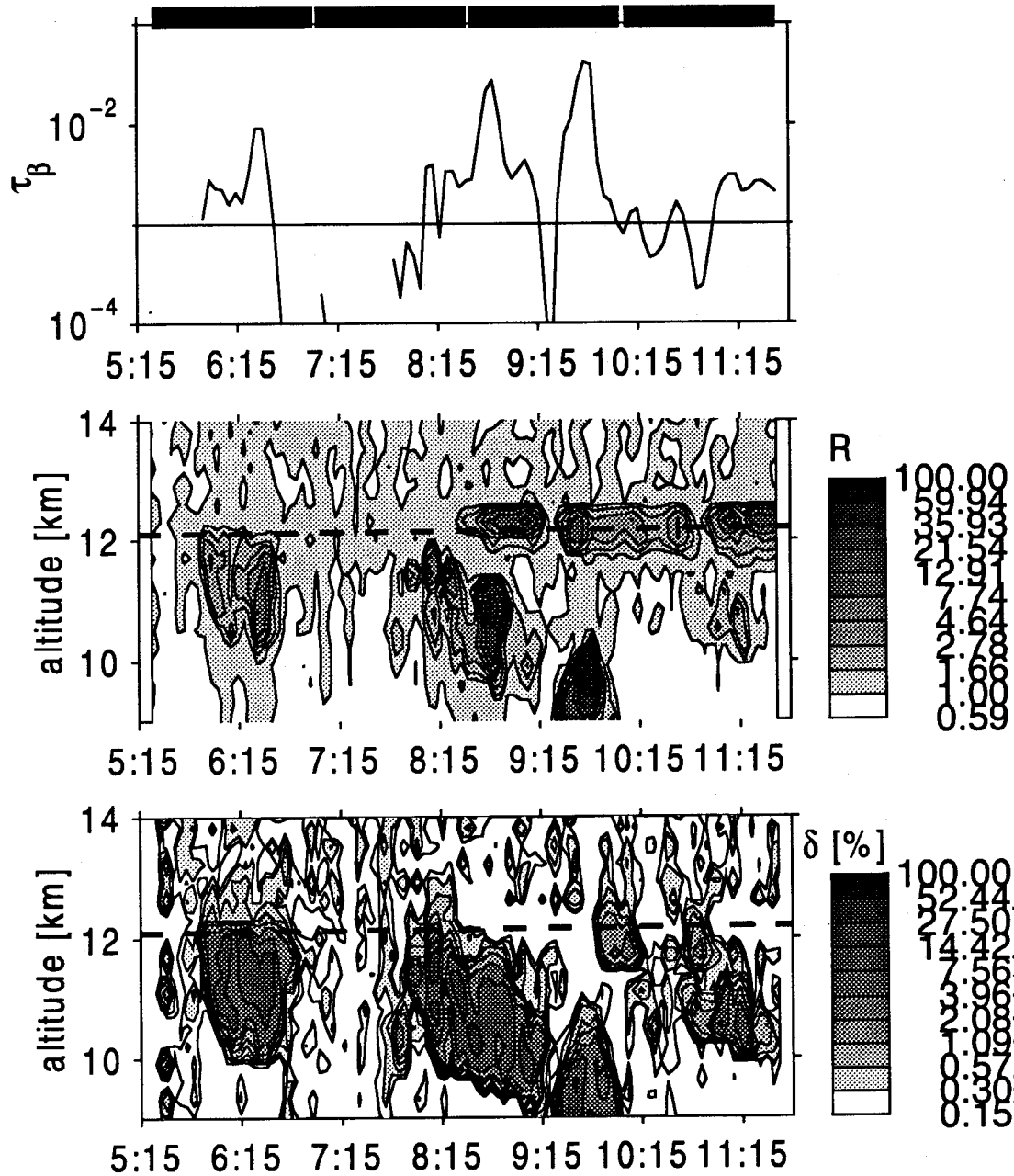


Figure 5. Temporal and spatial evolution of backscatter ratio (middle) and volume depolarization (bottom) at 532 nm as observed by TAL during 13 March 1997. The temperature tropopause derived from NCEP data is marked by dashed lines. The top panel shows the corresponding integrated aerosol backscatter coefficient. The dotted line indicates a subvisibility threshold of 10^{-3} sr^{-1} . See text for details.

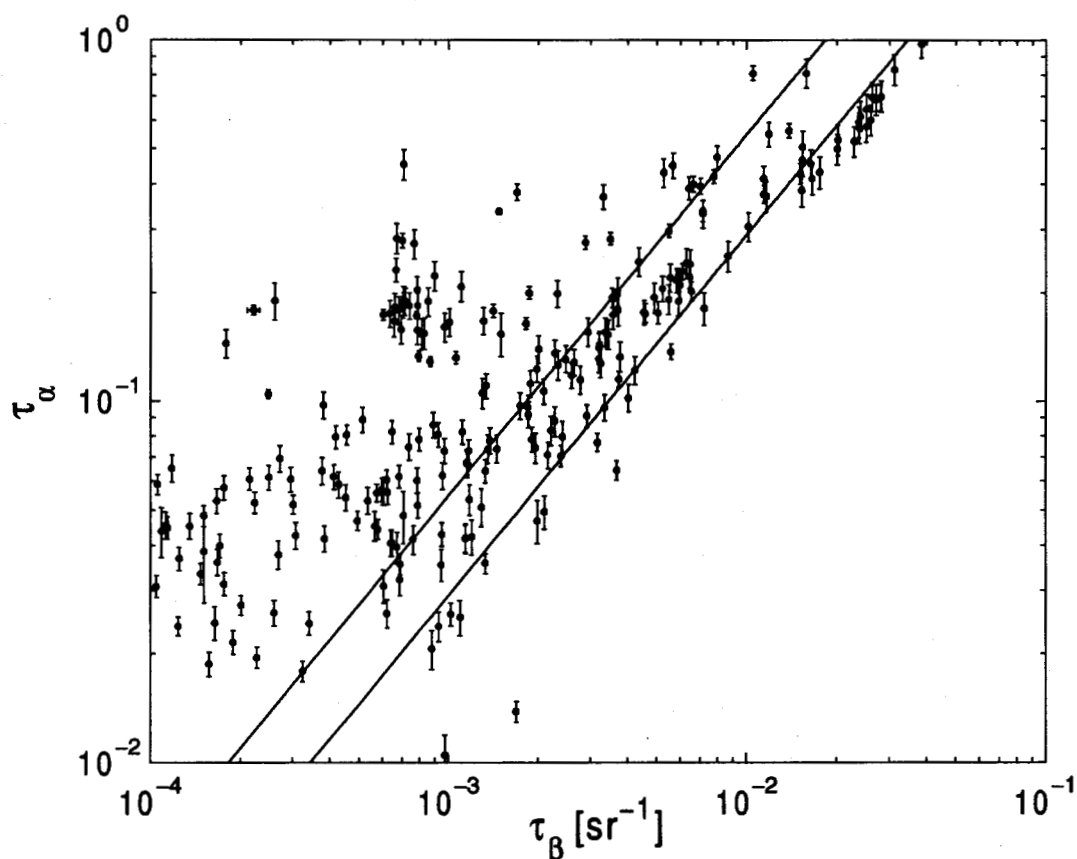


Figure 6. Relationship between the integrated aerosol backscatter coefficient and optical depth of cirrus clouds at 532 nm. The integration was performed between 9 and 14 km altitude. The linear fit for τ_β exceeding 10^{-2} sr^{-1} and 10^{-4} sr^{-1} yields column lidar ratios of 30 sr (dashed line) and 45 sr (full line), respectively.

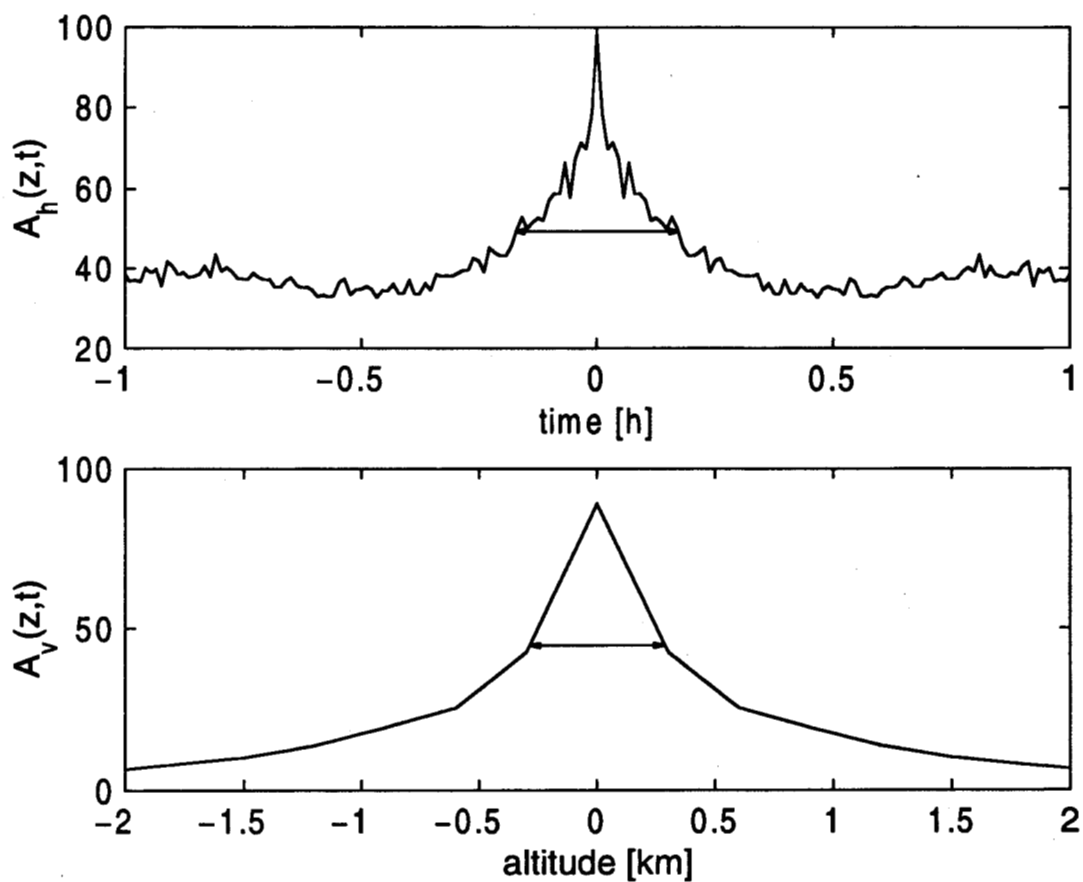


Figure 7. Mean auto-correlation functions of TAL cirrus measurements in vertical (top) and horizontal (bottom) direction. The functions $A_v(z,t)$ and $A_h(z,t)$ are calculated from backscatter ratio profiles at altitude between 8 and 14 km. The FWHMs (marked by the arrows) are 562 m and 20.6 min, respectively.

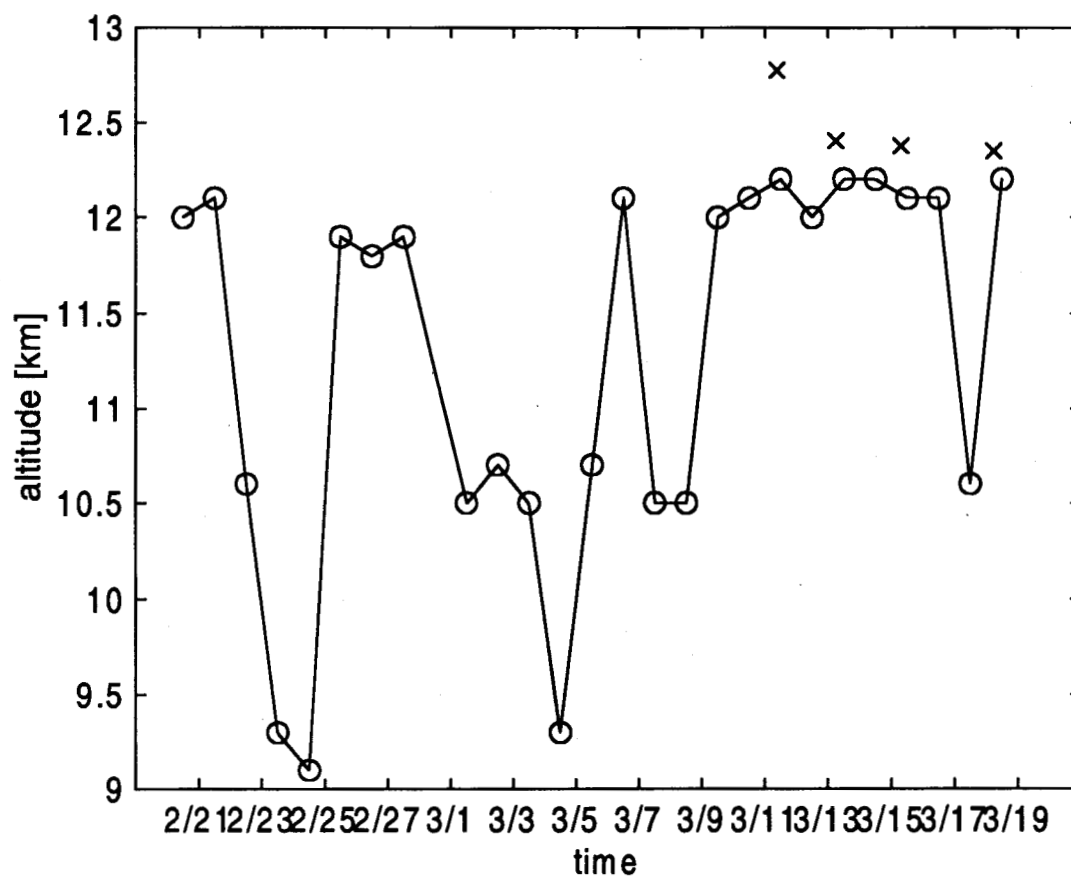


Figure 8. Tropopause altitudes derived from NCEP temperature profiles (circles). Altitudes obtained by the four in-situ temperature measurements are marked by crosses. The differences between NCEP and in-situ tropopause altitudes vary between 250 and 590 m.

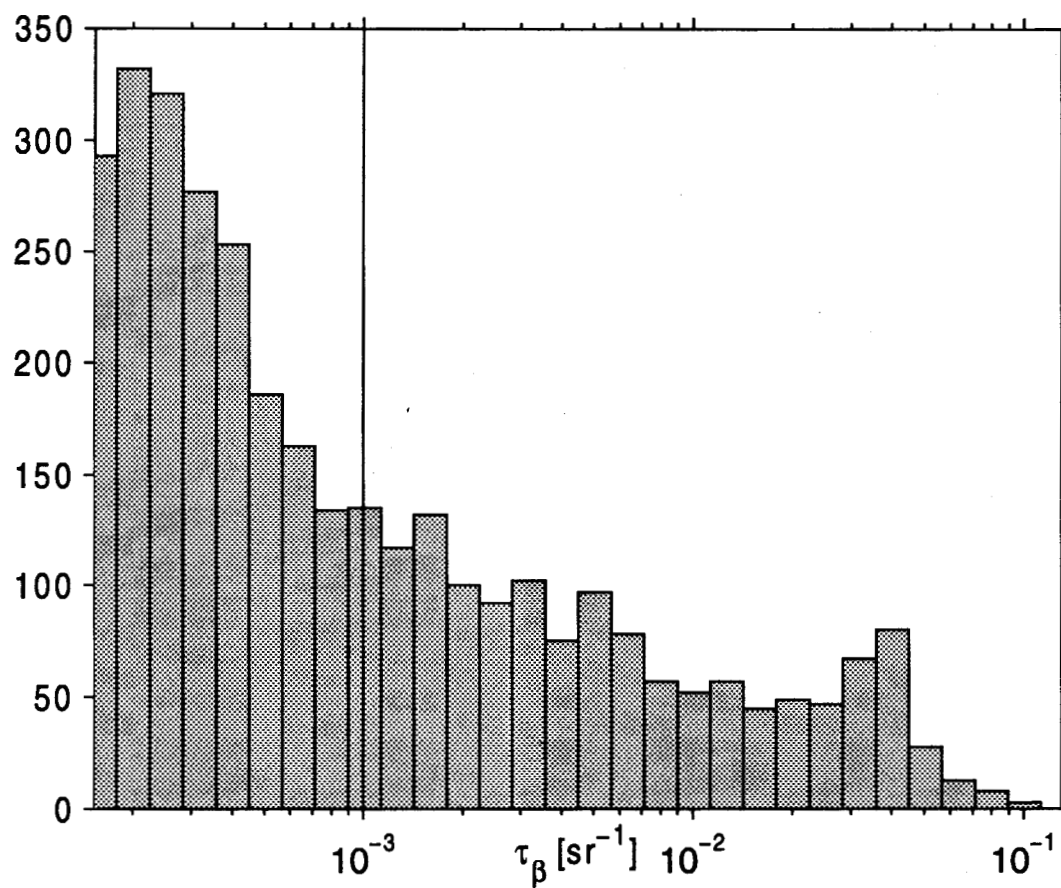


Figure 9. Occurrence distribution of integrated backscatter τ_β at 532 nm. τ_β is calculated for the altitude range 9–14 km from TAL observations. The subvisibility threshold of 10^{-3} sr^{-1} is marked by a dotted line.

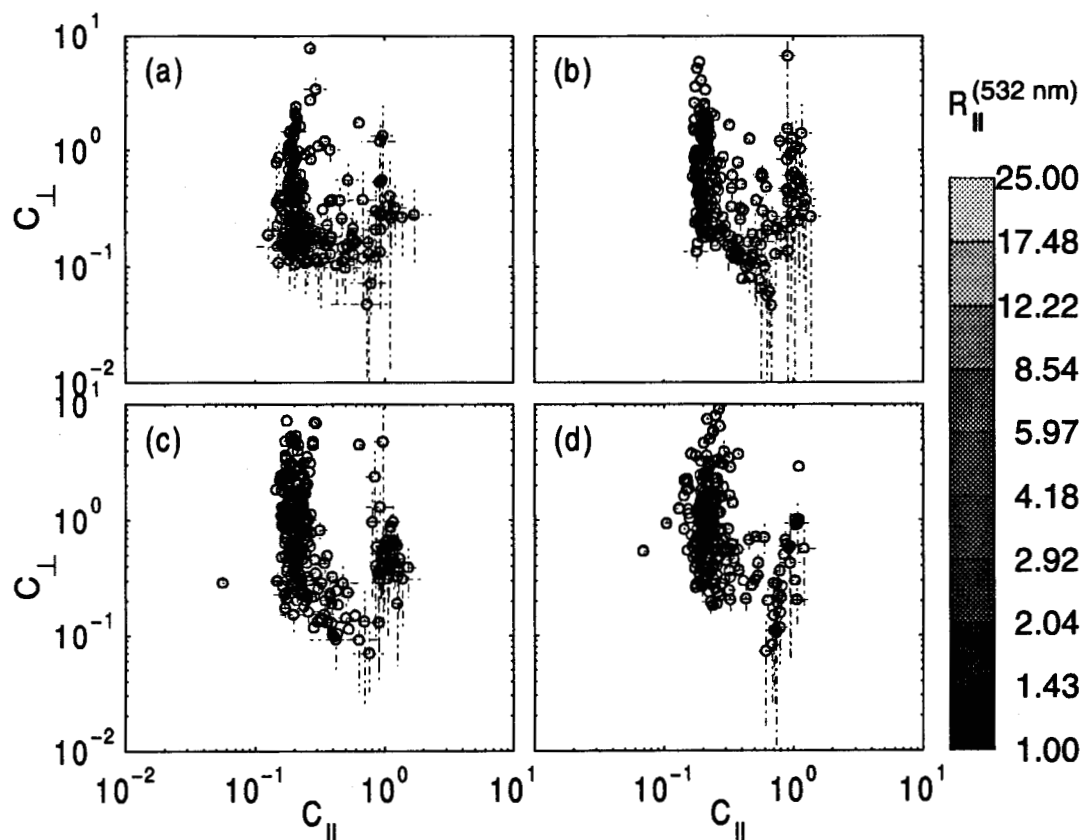


Figure 10. The relationship between the parallel color ratio $C_{||}$ and the perpendicular color ratio C_{\perp} derived from the lidar observations. The individual plots show the relationship for temperature ranges of 195–210 K (a), 210–225 K (b), 225–240 K (c), and 240–255 K (d).

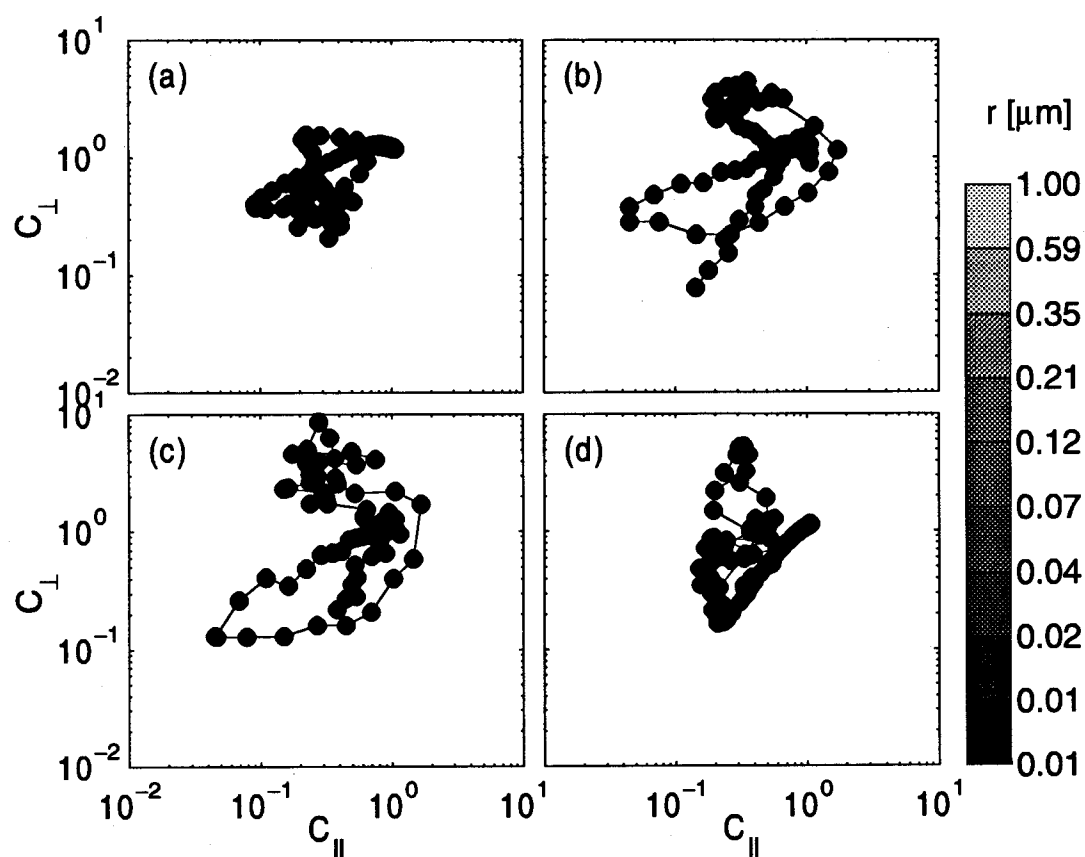


Figure 11. The relationship between the parallel color ratio C_{\parallel} and the perpendicular color ratio C_{\perp} derived from T-matrix calculations. The calculations were performed with aspect ratios of 0.5 (a), 0.8 (b), 1.25 (c), and 2.5 (d).

Tables

emitted wavelengths	: 532 and 351 nm
detected wavelengths	: 532, 382, and 351 nm
detection channels	: 351 nm
	: 382 nm
	: 532 nm
laser type	: XeF, Nd:YAG
pulse repetition frequency	: 50 Hz at 532 nm, 200 Hz at 351 nm
pulse energy	: 300 mJ at 532 nm
	100 mJ at 351 nm
beam expansion	: 5x (532 nm), 1x (351 nm)
telescope	: 0.91 m, f/2.5
field of view	: 1.9 mrad
detection mode	: photon counting
dwel time	: 1 or 2 μ sec

Table 1. Technical details of the AT-lidar instrument.

emitted wavelengths	: 532 and 355 nm
detected wavelengths	: 607, 532, 387, and 355 nm
depolarization channel	: 532 and 355 nm
detection channels	: 355 nm \parallel , 355 nm \perp , 387 nm \parallel (N ₂) 408 nm \parallel (H ₂ O), 532 nm \parallel , near, 532 nm \parallel , far 532 nm \perp , 607 nm \parallel (N ₂)
filter full width half maximum (FWHM)	: 5 nm (355 nm) 6 nm (387 nm, 408 nm) 10 nm (532 nm) 9 nm (607 nm)
laser type	: Nd:YAG
pulse repetition frequency	: 30 Hz
pulse energy	: 280 mJ at 532 nm 360 mJ at 355 nm
beam divergence (before expansion)	: 1 mrad
trans. beam expansion	: 9x
receiver telescope type	: Pressman-Camichel
receiver telescope diameter	: 1.14 m
overall f number	: 1/3.1
rec. telescope FOV	: 0.2 mrad
detection mode	: photon counting and analog detection
PMT types	: Burle 8850, EMI 9893, and EMI 9863
dwel time	: 800 nsec (photon counting)
digitizer frequency	: 20 MHz (analog mode)

Table 2. Technical details of the MARL instrument.

emitted wavelengths	: 1064, 532, and 355 nm
detected wavelengths	: 1064, 532, 387, and 355 nm
depolarization channel	: 532 nm
detection channels	: 355 nm
	387 nm (N ₂)
	532 nm
	532 nm ⊥
	1064 nm
laser type	: Nd:YAG
pulse energy	: 400 mJ at 532 nm
	300 mJ at 355 nm
pulse repetition frequency	: 10 Hz
beam divergence	: 1 mrad
rec. telescope	: Newton
rec. telescope diameter	: 0.4 m
rec. telescope FOV	: > 10 mrad
FWHM of IF-filters	: 1 nm (532 nm)
	2 nm (355 nm)
	5 nm (1064 nm)
detection mode	: photon counting
photomultiplier	: EMI 9813, EMI 9883, and
	Hamamatsu H5783P-06 (532 nm,)
preamplifier	: Phillips Scientific 6950 (532 nm,)
discriminator	: Phillips Scientific 6904
multi channel scaler	: Oxford MCS II
dwel time	: 2 μsec

Table 3. Technical details of the TAL instrument.

light source	: Xe flash lamp
emitted light energy	: 7 J per pulse
detected wavelengths	: 940 and 490 nm
filter width	: about 150 nm
pulse repetition frequency	: about 1/7 Hz
height resolution	: 25–35 m
detectors	: photodiodes
SNR	: about 100 at 20 km
additional sensors	: temperature pressure ozone partial pressure rel. humidity
weight	: 7 kg
balloon volume	: 1500 m ³

Table 4. Technical details of the backscatter sonde.

date	AT-lidar	MARL	TAL	sonde	cirrus
2/19/97		10:11 – 14:01	7:46 – 11:27		×
2/20/97		5:13 – 12:53	3:09 – 8:48		×
2/21/97		5:54 – 14:06	5:44 – 13:01		×
2/22/97		2:37 – 13:38	5:22 – 13:42		×
2/23/97		4:59 – 13:55	2:43 – 12:19		
2/24/97		2:45 – 14:06	3:51 – 11:12		
2/25/97		6:37 – 12:31	6:23 – 9:25		
2/27/97		4:16 – 7:54	3:50 – 8:01		×
3/ 1/97		2:28 – 12:53	3:26 – 9:34		
3/ 2/97	5:08 – 8:05	2:45 – 12:50	3:56 – 10:13		×
3/ 3/97	2:55 – 6:01	4:27 – 13:26	6:05 – 12:18		×
3/ 4/97	4:01 – 8:25	4:40 – 14:17	4:00 – 10:27		×
3/ 5/97	3:25 – 6:59	3:20 – 13:42	6:46 – 12:59		×
3/ 6/97	4:47 – 8:25	4:41 – 13:29	4:35 – 10:48		
3/ 7/97	4:30 – 9:55	4:18 – 13:46	7:08 – 11:44		
3/ 8/97	4:30 – 6:31	3:14 – 13:45	9:07 – 12:10		
3/ 9/97	5:40 – 7:55	4:58 – 12:38	3:35 – 12:16		
3/10/97	4:15 – 7:38	4:42 – 12:59	3:17 – 12:54		×
3/11/97	4:35 – 11:06	3:05 – 13:55	5:50 – 13:06	8:54 – 10:20	×
3/12/97	4:05 – 7:55	3:57 – 13:44	3:13 – 10:35		×
3/13/97	4:02 – 8:24	2:56 – 14:05	5:23 – 11:35	6:06 – 7:31	×
3/14/97		3:18 – 13:58			×
3/15/97		3:31 – 14:03	5:42 – 10:16	7:10 – 8:42	×
3/16/97		4:11 – 7:13	5:48 – 9:44		×
3/18/97			5:11 – 10:08	6:01 – 7:31	
total	44.5 h	217.7 h	151.4 h		

Table 5. Listing of measurements and backscatter sonde soundings. Times and dates are given in UTC. The occurrence of cirrus layers is marked in the last column.